IET Power Electronics

Research Article

IET Journals
The Institution of Engineering and Technology

Design of a wireless charging system with a phase-controlled inverter under varying parameters

ISSN 1755-4535
Received on 20th April 2015
Revised on 30th July 2016
Accepted on 18th August 2016
doi: 10.1049/iet-pel.2015.0275
www.ietdl.org

Qijun Deng[1], Jiangtao Liu[2] ✉, Dariusz Czarkowski[3], Mariusz Bojarski[3], Erdem Asa[3], Francisco de Leon[3]

[1]*Department of Automation, Wuhan University, Wuhan 430072, People's Republic of China*
[2]*Department of Physics and Electrical Engineering, Hubei University of Education, Wuhan 430205, People's Republic of China*
[3]*Department of Electrical and Computer Engineering, NYU Tandon School of Engineering, Brooklyn, New York 11201, USA*
✉ *E-mail: Liu_jiangtao@whu.edu.cn*

Abstract: Class-D full bridge is the most common inverter topology at the primary side for wireless electric vehicles (EVs) charging systems. This study takes a novel topology of a phase-controlled inverter as the power amplifier and puts it in a context of the whole charging system. The proposed inverter topology regulates the charging power through adjusting the phase-shift angle among phases with a constant operating frequency, which alleviates the EMI filter design. For various wireless EVs chargers, the gaps between the primary side and the secondary side are changing, which results in various coupling factors k. The equivalent resistance of the EVs battery R_{battery} is also changing during the charging process. Even resonant frequencies at two sides are variable because of the components tolerances and operating environments. This study presents design considerations of a wireless EVs charging system with the proposed technology under variable k, R_{battery}, and resonant frequencies. Circuit parameters are designed and the system efficiency is derived. Industrial prototype of an EV charging system is manufactured with the proposed topology at 3.0 kW. Experiments show that these design considerations can reflect the system characteristics, and the proposed system is a good candidate to be used in wireless EV battery chargers.

1 Introduction

Currently, the most common charger for electric vehicles is a plug-in station. This means that consumers must insert a plug into a receptacle on the car to charge batteries. The charging power ranges from 1.5 kW (slow charging) to a few tens of kW's (fast charging). Another recommended method is to replace used-out batteries. The first method presents an inconvenience and danger of connecting cars with cables to power grid or an off-board charger, and the secondary method is costly and requires a special infrastructure. In contrast with the above, the wireless charging system has several advantages including convenience, weather proof, anti-vandalism, and low risk of hazards. Therefore, numerous research projects were carried out to implement efficient [1–6], flexible [7–12], high power rate [5, 12–14] and controllable [12, 15, 16] wireless charging systems.

The wireless charging system is based on magnetic resonant coupling. The system contains a primary coil mounted under the parking space ground and a secondary coil fixed on the vehicle chassis. These two coils exchange power through an alternating electromagnetic field. Adjustable output power at the primary side is an important issue for actual wireless EV charging systems. Currently, most researches take the class-D bridge topology as the power amplifier and the frequency control is employed to regulate the output power at the primary side [2–4]. In [16, 17], an LCL-T-based, multiple modules parallel power supply is used to provide adjustable output power for the primary side coil, but the introducing of transformers decreases the available inductance coupled with the secondary side. Cai *et al.* [18] depict a harmonic-based phase-shifted control topology for the IPT power supply, which is dedicated to light output power conditions. A SiC-based matrix converter topology is introduced in [19], but its efficiency is somewhat low (85%). In addition, the requirement of input DC voltage for inverters, and MOSFET switching conditions with considering the varying of parameters, including coupling factors, resonant frequencies at both sides, and loads, are not thoroughly investigated in above IPT power supplies.

Phase-controlled inverters have shown many advantages compared with class-D topologies [12, 20–23]. For a certain required output current at the primary side, an N-phase phase-controlled inverter decreases the current through each switch to about $1/N$ of a single-phase bridge inverter. Hence, multi-phase phase-controlled inverters are especially suitable for high power applications. Bojarski *et al.* [12] present a 25 kW prototype with three-phase phase-controlled inverter. Moreover, the phase-controlled inverter can regulate the output power through adjusting the phase-shift angle among phases with a constant operating frequency, which decreases the difficulty of EMI filter design. As to wireless charging systems, properly designed multiple-phases phase-controlled inverters show higher efficiencies on some charging stages comparing with single-phase class-D topologies.

For a stable and efficient operation, a wireless charging system should be able to match different vehicles with various heights of chasses at different stages of the charging process. This translates into various coupling factors between the two coils and a variable equivalent resistance of batteries which affects the load condition of the inverter. Moreover, the circuit parameters are always different from the nominal ones because of components tolerances and operating environments.

Different from [12] which focuses on the high power level, this paper studies the possibility to put the topology in a context of the whole charging process as well as varying air gap. The paper is organised as follows: Section 2 describes basic circuits of the wireless charging system. Section 3 describes the design process to determine parameters of the system under various coupling factors, load conditions, and resonant frequencies. Section 4 focuses on the input DC voltage design and analyses the system efficiency based on designed parameters. Finally, experimental results are provided to validate the design method and conclusions are drawn.

2 Basic circuits of the wireless charging system

There are several types of circuit topologies proposed for primary and secondary sides of a wireless power transfer (WPT) system [1–5]. This paper takes the most common class-D series resonant circuit and employs a phase-controlled inverter with a 50% duty cycle at the primary side [12, 20–23]. In contrast with the class-D full-bridge inverter [2, 4], the phase-controlled inverter has a smaller current through each switch under a given output power. At the secondary side, a series resonant circuit with a class-D full-bridge rectifier is selected. The topology of the system is shown in Fig. 1 where the DC input voltage V_I is provided by the rectifier of a power factor correction circuit, which will not be detailed here.

The primary side consists of a phase-controlled inverter (which includes three half-bridge inverters in parallel and three inter-cell transformers ICT_1 through ICT_3), a resonant capacitor C_P, a resonant inductor L_P (the primary coil) and an equivalent resistance R_P that is the sum of equivalent series resistances (ESR's) of the coil and the capacitor. The inter-cell transformer (ICT) provides useful functions such as isolation, filtering, and inter-cell coupling [23]. Every inter-cell transformer consists of two windings, connected between half-bridge switching legs (namely, cells), as shown in Fig. 1.

The secondary side comprises a resonant inductor L_S (secondary coil), a resonant capacitor C_S, a full-bridge rectifier, a filter capacitor C_f, and battery packs represented by a source $V_{battery}$.

The phase-controlled inverter can regulate the input voltage (namely $\boldsymbol{V}_Z$ in Fig. 1) of the resonant circuit through adjusting angles among three half-bridge inverters. This means that it can adjust the charging power of batteries without changing the operating frequency.

2.1 Output voltage and phase currents of phase-controlled inverter

Considering inter-cell transformers ICT_1 through ICT_3, the magnetising inductance at primary sides and secondary sides are L_{1P} through L_{3P} and L_{1S} through L_{3S}, respectively. It is assumed that all of the windings have the same magnetising inductance, leakage inductance and ESR. Then, the winding impedance of each inter-cell transformer is equivalent to the sum of the magnetising inductance L_{mag}, one half of the leakage inductance L_{leak} and the ESR r_{ICT}. Since each phase current of the phase-controlled inverter flows through two windings, the circuit of Fig. 1*a* can be simplified as shown in Fig. 1*b*, where $\boldsymbol{V}_1$, $\boldsymbol{V}_2$, and $\boldsymbol{V}_3$ are the fundamental components of the output voltages from three inverters, respectively. These voltages are referenced to the negative side of V_I and expressed per (1), where φ is the phase-shift angle among half-bridge inverters [12, 20–23]

$$\begin{aligned}\boldsymbol{V}_1 &= \frac{2V_I e^{j\varphi}}{\pi}\\ \boldsymbol{V}_2 &= \frac{2V_I}{\pi}\\ \boldsymbol{V}_3 &= \frac{2V_I e^{-j\varphi}}{\pi}\end{aligned} \tag{1}$$

The voltage and current at the output of the phase-controlled inverter are expressed by (2) and (3) [22, 23], respectively,

$$\boldsymbol{V}_Z = \frac{2V_I(e^{j\varphi}+1+e^{-j\varphi})\boldsymbol{Z}_P}{\pi(\boldsymbol{Z}_b+3\boldsymbol{Z}_P)} = \frac{2V_I\boldsymbol{Z}_P(1+2\cos\varphi)}{\pi(\boldsymbol{Z}_b+3\boldsymbol{Z}_P)}, \tag{2}$$

$$\boldsymbol{I}_P = \boldsymbol{V}_Z/\boldsymbol{Z}_P = \frac{2V_I(1+2\cos\varphi)}{\pi(\boldsymbol{Z}_b+3\boldsymbol{Z}_P)}, \tag{3}$$

where $\boldsymbol{Z}_b$ is the impedance of each phase of the phase-controlled inverter, $\boldsymbol{Z}_P$ is the load impedance of the phase-controlled inverter, and ω is the operating angular frequency. Equation (3) shows that the output current can be regulated through adjusting shift angles between phases. Section 4 shows that the power of the secondary side is also regulated by the angles. Equation (4) shows formulas for calculation of parameters used in (2) and (3)

$$\begin{aligned}\boldsymbol{Z}_b &= j\omega L_{leak} + r_{MOS} + 2r_{ICT}\\ \boldsymbol{Z}_P &= R_P + j\omega L_P + 1/j\omega C_P + \boldsymbol{Z}_{Sreflect}\\ \boldsymbol{Z}_{Sreflect} &= (\omega M)^2/\boldsymbol{Z}_S = (\omega k)^2 L_P L_S/\boldsymbol{Z}_S\\ \boldsymbol{Z}_S &= R_s + j\omega L_s + 1/j\omega C_s\\ R_s &= R_{equi} + r_{ESR}\end{aligned} \tag{4}$$

The inductance of the inter-cell transformer is separated into the magnetising inductance L_{mag} and the leakage inductance L_{leak}. $\boldsymbol{Z}_{Sreflect}$ is the equivalent impedance that the secondary side reflects to the primary side, $\boldsymbol{Z}_S$ is the impedance of the secondary side and R_S is its real part, R_{equi} is the input resistance of the secondary side rectifier whose expression will be derived in Section 2.1, r_{ESR} is the equivalent on-resistance of the secondary side and ω_0 is the resonant angular frequency of the circuit.

In order to calculate the power loss of the phase controlled inverter, an expression for the current of each phase should be derived. Based on the current calculation method proposed in [23], these currents can be expressed as

$$\begin{aligned}\boldsymbol{I}_1 &= \frac{1}{3}\left(\boldsymbol{I}_P + \frac{2\boldsymbol{V}_1 - \boldsymbol{V}_2 - \boldsymbol{V}_3}{2j\omega L_{mag} + j\omega L_{leak}}\right)\\ \boldsymbol{I}_2 &= \frac{1}{2}\left(\boldsymbol{I}_P - \boldsymbol{I}_1 + \frac{\boldsymbol{V}_2 - \boldsymbol{V}_3}{2j\omega L_{mag} + j\omega L_{leak}}\right)\\ \boldsymbol{I}_3 &= \boldsymbol{I}_P - \boldsymbol{I}_1 - \boldsymbol{I}_2.\end{aligned} \tag{5}$$

2.2 Rectifier input resistance at the secondary side

There is a full-bridge rectifier at the secondary side. Assuming that the current wave of the secondary is a sinusoid and the filter capacitance is big enough that the ripple of the current through the battery can be ignored, and the current through the battery $I_{battery}$ is equal to the average of the secondary side current, which can be expressed as

$$I_{battery} = \frac{1}{\pi}\int_0^{\pi} I_S \sin(\omega t)\,d\omega t = \frac{2I_S}{\pi}, \tag{6}$$

where I_S is the amplitude of the secondary side current. Since the equivalent resistance R_{equi} consumes the same power as the battery nominal load resistance $R_{battery}$, the following is true:

$$I_S^2 R_{equi}/2 = I_{battery}^2 R_{battery} \tag{7}$$

Combination of (6) and (7) leads to the equivalent resistance R_{equi} as

$$R_{equi} = \frac{8R_{battery}}{\pi^2}. \tag{8}$$

3 Design of the system parameters

3.1 Resonant frequency and operating frequency

According to the standard of SAE TIR J2954, the band of 85 kHz is selected for the light duty vehicle WPT, which provides an operation

IET Power Electron., 2016, Vol. 9, Iss. 13, pp. 2461–2470

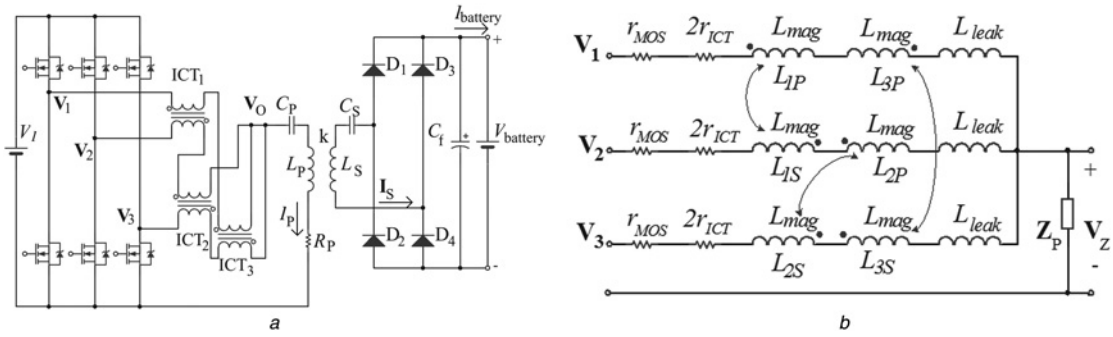

Fig. 1 *Topology and its equivalent circuit of the analysed wireless charging system*

a Topology
b Equivalent circuit

frequency range from 81.38 to 90 kHz. Hence 88 kHz is selected as the operating frequency f_{OP}. The operating frequency should be above the resonant one to obtain zero voltage switching (ZVS) for MOSFETs. For a resonant circuit with an inductive load, a higher operating frequency results in a lower output current and power. Hence, the operating frequency should not be much higher than the resonant one. Taking the above into consideration, a frequency of 82 kHz is employed as the resonant frequency f_{resP} for circuit designs at the primary side. With respect to the secondary side, the resonant frequency f_{resS} for parameters design is 91 kHz, which contributes an inductive impedance to the primary side and benefits the ZVS operation for MOSFETs. Actually, the ZVS state will be lost at low load resistances together with large coupling factors if the secondary side employees a lower resonant frequency, e.g. 88 kHz. The ZVS condition can be obtained when the current lags the voltage of inverters, i.e. inverters have inductive loads. At the end of this section, ZVS condition will be checked under given designed parameters.

3.2 Battery equivalent resistance

The battery behaves as a resistive load when it is being charged. The equivalent resistance of the battery packs $R_{battery}$ is defined as

$$R_{battery} = V_{battery}/I_{battery}. \tag{9}$$

$R_{battery}$ can be obtained through a cable charging experiment. The charging process is divided into three stages, namely the constant current, the constant power, and the constant voltage one. A simple bang-bang control is employed in this experiment to regulate the charging current, voltage, and power through adjustment of the phase-shift angle. The battery charging current and voltage are measured once every half an hour during the cable charging experiment, then $R_{battery}$ is calculated per (9). The charging power is calculated according to the expression $P_{battery} = V_{battery}\ I_{battery}$. These parameters in a typical charging process are listed in Table 1.

3.3 Coil dimensions and coupling factors

Mutual inductance between two coils can be expressed by the product of the coil area and the field intensity. A larger cross-section area means lower field intensity for a given mutual inductance. In order to decrease the magnetic field intensity to meet safety standards of human body exposure in vehicles, a larger cross-sectional area with fewer turns is preferred to a smaller cross-sectional area with more turns. The largest radius is, however, limited by the dimension of the vehicles. Two coils of the same dimensions, namely 4-turn planar rectangular spiral ones with 90 cm × 70 cm outer dimensions, are employed for either side. The litz wire winding the coils is AWG38, 2000 wires with an outer diameter of 6 mm. The centre-to-centre space between two adjacent coil turns is 1 cm. According to a *Maxwell* software simulation, the inductances of both coils are about 33.7 μ□. The preferred inductance value can be obtained through adjusting the space between two adjacent turns. Considering the litz wire DC resistance of 0.36 Ω per 1000 ft (according to the specification of the manufacturer), the coil resistance under designed dimensions is about 0.02 Ω. When the contribution of the skin and proximity effects is counted at 88 kHz, an additional resistance which is approximately equal to the DC one, namely, 0.02 Ω is suitable for following designs, which leads to the total coil resistance of 0.04 Ω [24].

It is assumed in this paper that the minimum distance between the primary and the secondary coils is 12 cm and the maximum one is 25 cm. As a result, the coupling factor k changes from 0.34 to 0.19 according to *Maxwell* software simulations.

3.4 ZVS condition of inverters

The equivalent impedance is calculated in (10) and the phase angles θ_i that the current lags the voltage can be derived from the real and imaginary parts of the impedance

$$\boldsymbol{Z}_i = \boldsymbol{V}_i/\boldsymbol{I}_i, \quad i = 1, 2, 3, \tag{10}$$

where $\boldsymbol{V}_i$ and $\boldsymbol{I}_i$ are calculated per (1) and (5), respectively. Equation (2) shows that when the phase-shift angle φ varies from 0° to 120°, the output voltage (hence, the output power) changes from the maximum to zero. Fig. 2 shows the simulated phase angle θ_i plots of three inverters versus the phase-shift angle among phases when $k = 0.226$, $R_{battery} = 7\ \Omega$, $f_{resP} = 82$ kHz, $f_{resS} = 91$ kHz and $f_{OP} = 88$ kHz. The minimum phase angle of three inverters [namely, min (θ_i)] under above parameters is 18.7°. Fig. 3*a* depicts the surface of min(θ_i) under above frequencies, various k and $R_{battery}$.

In wireless EV charging systems, realistic parameters may be different from the designed ones. The resonant frequencies deviate from the designed ones because of both components tolerances and operation environments. Moreover, comparing with the ones listed in Table 1, the equivalent battery resistance may be even lower at the beginning of the constant current stage and higher at the end of the constant voltage stage. In order to evaluate the effectiveness of the presented topology under a broader range of parameters, simulations are conducted under the following extended ranges of the resonant frequencies and resistance:

(a) the deviation range of resonant frequencies is ±2.5% for both sides, and
(b) the first and the last groups of parameters in Table 1 are replaced by 10 V, 20 A, 0.5 Ω, 40 W, and 173.3 V, 2.89 A, 60 Ω, 500 W, respectively.

There are infinite combinations under the range of the previous resonant frequencies. Simulations of the min(θ_i) are conducted

Table 1 17 Groups of parameters $V_{battery}$, $I_{battery}$, $R_{battery}$ and $P_{battery}$ from a cable charging process

$V_{battery}$, V	140.3	145.5	148.3	150.4	152.8	156.0	157.4	159.6	160.6	162.8	165.8	171.7	172.6	172.7	173.0	173.2	173.3
$I_{battery}$, A	20.04	19.99	19.89	19.85	19.80	19.31	19.10	18.96	18.84	18.55	18.10	15.24	10.65	8.19	6.98	6.12	5.70
$R_{battery}$, Ω	7	7.28	7.46	7.58	7.72	8.08	8.24	8.42	8.52	8.78	9.16	11.26	16.04	20.94	24.64	28.12	30.4
$P_{battery}$, W	2812	2908	2950	2986	3026	3012	3006	3026	3026	3020	3000	2616	1838	1414	1208	1060	988

under the extreme ones, and two of them are shown in Figs. 3*b* and *c*. It can be seen that under the broader resonant frequencies and resistances, the ZVS condition is still maintained.

4 Design of input DC voltage and efficiency analysis

The input DC voltage from PFC should be designed carefully to supply enough charging power for the battery. However, much higher DC voltage will result in higher rating parameter requirements for PFC. In order to find out the proper DC voltage, power loss should be considered firstly.

4.1 Power loss of the primary side

The power loss of the primary side includes conduction losses and switching losses. The conduction losses for each switch, the resonant capacitor, the resonant inductor (the primary coil) and each inter-cell transformer are $P_{SW}(i)$, P_{CP}, P_{LP} and $P_{ICT}(i)$, respectively. Switching losses consist of turn-on and turn-off loss $P_{SSW}(i)$. The operating frequency is 110% of the resonant frequency, which ensures switches running at zero-voltage-switching. Hence, the turn-on loss is zero and only turn-off loss is calculated. All of these losses are listed, respectively, in (11) [20] as

$$\begin{aligned} P_{SW}(i) &= \frac{I_i^2 r_{MOS}}{2}, \quad i = 1, 2, 3 \\ P_{CP} &= \frac{I_P^2 r_{CP}}{2} \\ P_{LP} &= \frac{I_P^2 r_{LP}}{2} \\ P_{ICT}(i) &= \frac{(I_{m1(i)}^2 + I_{m2(i)}^2) r_{ICT(i)}}{2}, \quad i = 1, 2, 3 \\ P_{SSW}(i) &= \frac{\omega(t_r/3 + t_f/2) V_I I_i \sin\theta_i}{2\pi}, \quad i = 1, 2, 3, \end{aligned} \tag{11}$$

where $I_{m1(i)}$ and $I_{m2(i)}$ are the currents through two windings of the inter-cell transformer i, t_r and t_f are the raise time and fall time of MOSFETs, respectively.

Then the total conduction loss is

$$\begin{aligned} P_{Pconduct} &= \sum_{i=1}^{3} [P_{SW}(i) + P_{ICT}(i)] + P_{CP} + P_{LP} \\ &= (r_{MOS} + r_{ICT}) \sum_{i=1}^{3} I_i^2 + \frac{I_P^2 (r_{CP} + + r_{ICT})}{2}. \end{aligned} \tag{12}$$

The total switching loss is calculated per (13) as

$$\begin{aligned} P_{PSSW} &= \sum_{i=1}^{3} P_{SSW}(i) \\ &= \frac{\omega(t_r/3 + t_f/2) V_I (I_1 \sin\theta_1 + I_2 \sin\theta_2 + I_3 \sin\theta_3)}{2\pi}, \\ i &= 1, 2, 3, \end{aligned} \tag{13}$$

where the product $I_i \sin\theta_i$ is the turn-off current of each phase, and θ_i is the angle of the current lagging the voltage. Equation (10) gives the equivalent impedance of each inverter and θ_i can be calculated accordingly. The overall loss of the primary side is given by

$$P_{Ploss} = P_{Pconduct} + P_{PSSW}. \tag{14}$$

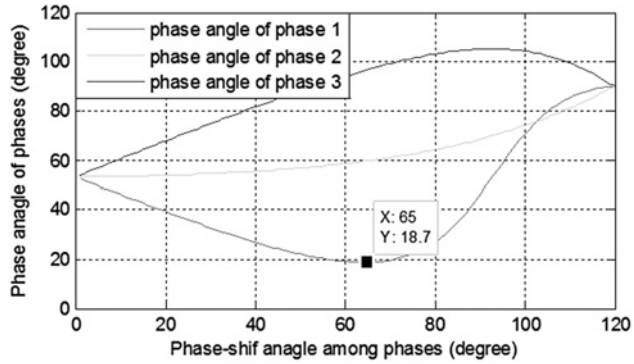

Fig. 2 *Simulation of the phase angle θ_i of three inverters versus phase-shift angle φ when k = 0.226, $R_{battery}$ = 7 Ω, f_{resP} = 82 kHz, f_{resS} = 91 kHz and f_{OP} = 88 kHz*

4.2 Power loss of the secondary side

The conduction losses at the secondary side consists of ones in the resonant capacitor P_{CS}, the resonant inductor (the secondary coil) P_{LS}, the rectifier diodes P_{RF}, and the filter capacitor P_{Cf}. In addition, the forward-voltage loss of rectifier diodes P_{VF} also contributes to the whole losses of the secondary side. Considering the rectifier bridge conduction loss calculation, the current goes through two series-connected diodes (D_1 together with D_4, or D_2 together with D_3) during half of the cycle, which can be equivalent to the current going through D_1 together with D_4 for the whole cycle while no current goes through D_2 together with D_3. Equations for these losses are given as follows [20]

$$\begin{aligned} P_{CS} &= \frac{I_S^2 r_{CS}}{2} \\ P_{LS} &= \frac{I_S^2 r_{LS}}{2} \\ P_{RF} &= \frac{I_S^2}{2} \times 2R_F = I_S^2 R_F \\ P_{Cf} &= \frac{I_S^2 r_{Cf}}{2}\left(\frac{\pi^2}{4} - 1\right) \\ P_{VF} &= 2V_F \times \frac{I_S}{\sqrt{2}} = \sqrt{2} V_F I_S \end{aligned} \tag{15}$$

where r_{Cf} is the ESR of the filter capacitor whose value is about 0.02 Ω and I_S is the amplitude of the secondary side resonant current given by

$$\boldsymbol{I}_S = \frac{\boldsymbol{V}_S}{\boldsymbol{Z}_S} = \frac{j\omega M \times \boldsymbol{I}_P}{\boldsymbol{Z}_S} = \frac{j\omega k\sqrt{L_S L_P}}{\boldsymbol{Z}_S} \times \frac{2V_1(1+\cos 2\varphi)}{\pi(\boldsymbol{Z}_b + 3\boldsymbol{Z}_P)}. \tag{16}$$

Equation (17) provides the whole power loss of the secondary side (see equation (17) at bottom of the next page)

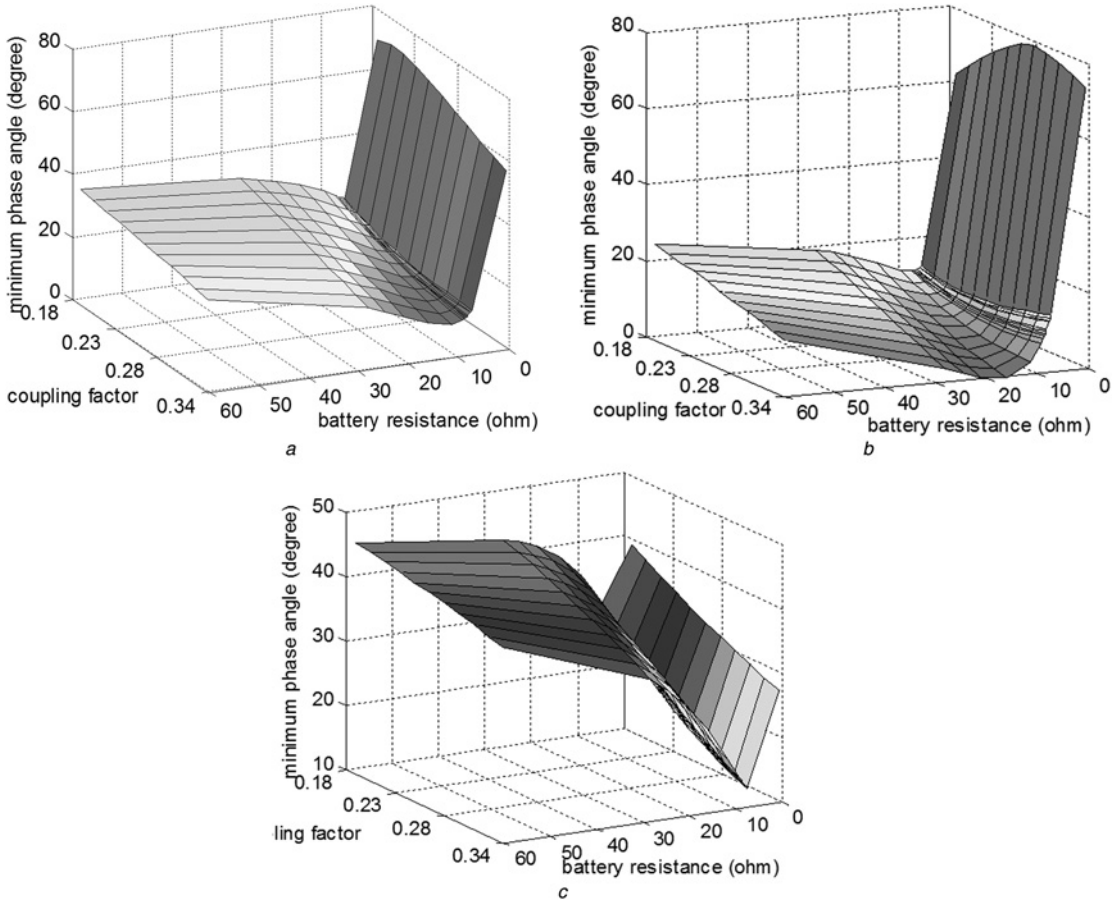

Fig. 3 *Simulation of the minimum phase angle surface versus coupling factor k and battery equivalent resistance $R_{battery}$*

a f_{resP} = 82 kHz, f_{resS} = 91 kHz, f_{OP} = 88 kHz, and $R_{battery}$ is from 7 to 30.4 Ω
b f_{resP} = 82 kHz × 102.5%, f_{resS} = 91 kHz × 102.5%, f_{OP} = 88 kHz, and $R_{battery}$ is from 0.5 to 60 Ω
c f_{resP} = 82 kHz × 97.5%, f_{resS} = 91 kHz × 97.5% and f_{OP} = 88 kHz, and $R_{battery}$ is from 0.5 to 60 Ω

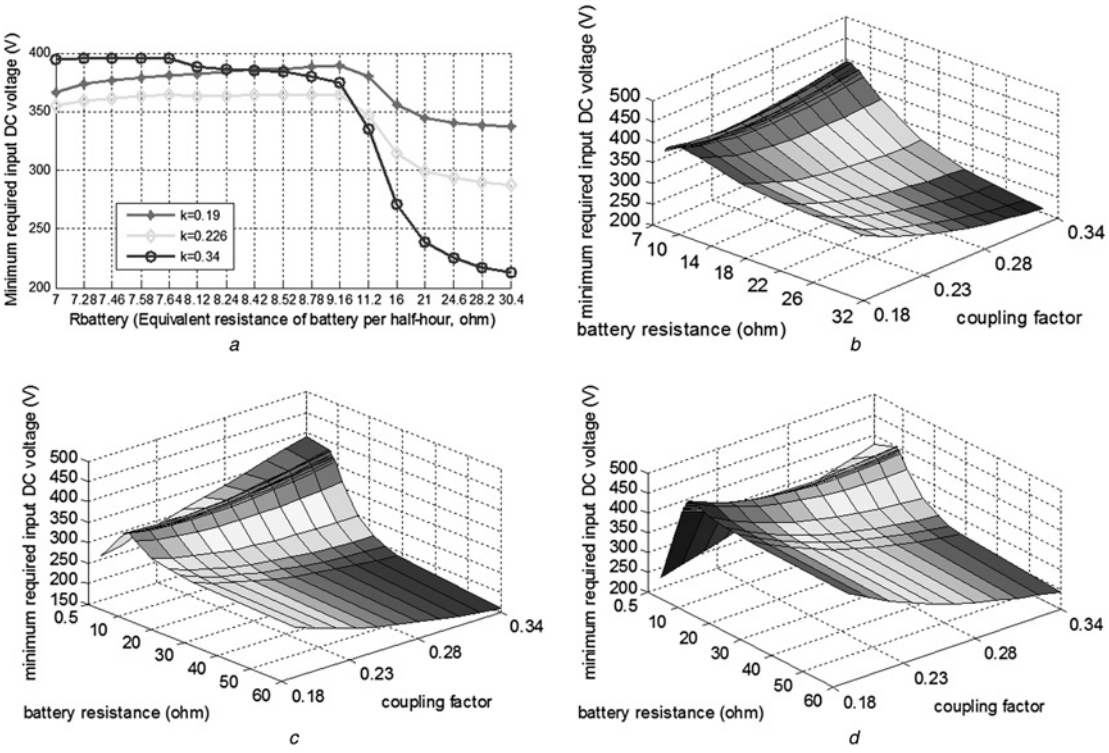

Fig. 4 *Simulation of the required input DC voltage versus coupling factor k and battery equivalent resistance $R_{battery}$*

a For three typical coupling factors *k*, $f_{resP} = 82$ kHz, $f_{resS} = 91$ kHz, $f_{OP} = 88$ kHz, and $R_{battery}$ is from 7 to 30.4 Ω
b For $f_{resP} = 82$ kHz, $f_{resS} = 91$ kHz, $f_{OP} = 88$ kHz, and $R_{battery}$ is from 7 to 30.4 Ω
c For $f_{resP} = 82$ kHz × 102.5%, $f_{resS} = 91$ kHz × 102.5%, $f_{OP} = 88$ kHz, and $R_{battery}$ is from 0.5 to 60 Ω
d For $f_{resP} = 82$ kHz × 97.5%, $f_{resS} = 91$ kHz × 97.5%, $f_{OP} = 88$ kHz, and $R_{battery}$ is from 0.5 to 60 Ω

4.3 Input DC voltage requirement

The total active power of the secondary side is equal to the active power consumed at the reflecting resistance of the secondary side to the primary side, which is shown as

$$P_S = \frac{I_P^2 \times \mathrm{Re}(Z_{Sreflect})}{2} = \frac{2V_I^2(1+2\cos\varphi)^2 \times \mathrm{Re}(Z_{Sreflect})}{\pi^2(\boldsymbol{Z}_b + 3\boldsymbol{Z}_P) \times \mathrm{Conj}(\boldsymbol{Z}_b + 3\boldsymbol{Z}_P)} = \frac{2V_I^2(1+2\cos\varphi)^2 \times \mathrm{Re}((\omega k)^2 L_P L_S/\boldsymbol{Z}_S)}{\pi^2(\boldsymbol{Z}_b + 3\boldsymbol{Z}_P) \times \mathrm{Conj}(\boldsymbol{Z}_b + 3\boldsymbol{Z}_P)}, \quad (18)$$

where I_P is the amplitude of the primary side current.

Defining

$$P_{S\varphi} = \frac{2\mathrm{Re}((\omega k)^2 L_P L_S/Z_S)}{\pi^2(\boldsymbol{Z}_b + 3\boldsymbol{Z}_P) \times \mathrm{Conj}(\boldsymbol{Z}_b + 3\boldsymbol{Z}_P)}, \quad (19)$$

Equation (18) can be changed into

$$P_S = P_{S\varphi} V_I^2 (1+2\cos\varphi)^2. \quad (20)$$

At the same time, the total active power of the secondary side can be expressed as a sum of the battery power and the total losses

$$P_S = P_{battery} + P_{Sloss} = \frac{V_{battery}^2}{R_{battery}} + \sqrt{2}V_F I_S + \frac{(2R_F + r_{CS} + r_{LS} + r_{Cf}(\pi^2/4-1))I_S^2}{2}, \quad (21)$$

Defining

$$I_{S\varphi} = \left| \frac{\mathrm{j}2\omega k\sqrt{L_S L_P}}{\pi(\boldsymbol{Z}_b + 3\boldsymbol{Z}_P)\boldsymbol{Z}_S} \right|$$
$$P_{srds\varphi} = I_{S\varphi}^2 \frac{(2R_F + r_{CS} + r_{LS} + r_{Cf}(\pi^2/4-1))}{2} \quad (22)$$
$$P_{VF\varphi} = \sqrt{2}V_F I_{S\varphi},$$

Equation (21) can be simplified to

$$P_S = \frac{V_{battery}^2}{R_{battery}} + P_{VF\varphi} V_I (1+2\cos\varphi) + P_{srdson\varphi} V_I^2 (1+2\cos\varphi)^2. \quad (23)$$

$$P_{sloss} = P_{VF} + P_{RF} + P_{CS} + P_{LS} + P_{CF} = \sqrt{2}V_F I_S + I_S^2 R_F + \frac{r_{CS} I_S^2}{2} + \frac{r_{LS} I_S^2}{2} + \frac{r_{Cf} I_S^2}{2}\left(\frac{\pi^2}{4} - 1\right) = \sqrt{2}V_F I_S + \frac{(2R_F + r_{CS} + r_{LS} + r_{Cf}(\pi^2/4-1))I_S^2}{2} \quad (17)$$

IET Power Electron., 2016, Vol. 9, Iss. 13, pp. 2461–2470

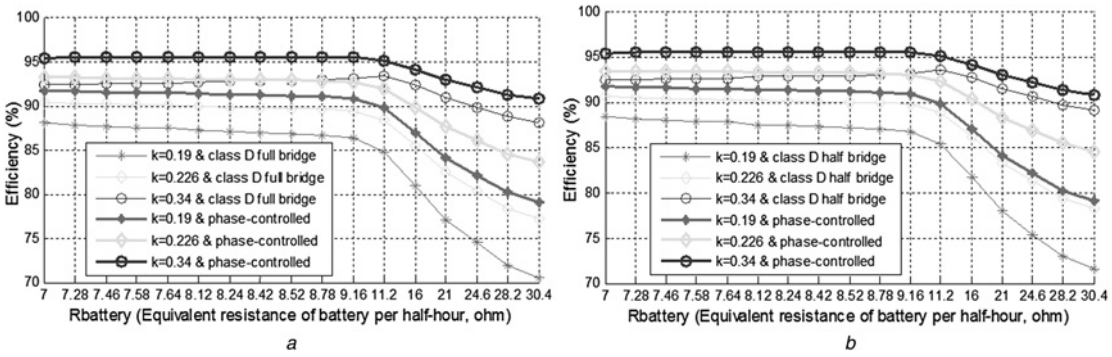

Fig. 5 *Simulation of charging efficiency comparison for the proposed topology with class-D topologies under nominal parameters*

a For full-bridge class-D topology
b For half-bridge class-D topology

Integrating (20) and (23) is transformed to

$$P_{S\varphi}V_I^2(1+2\cos\varphi)^2=\frac{V_{battery}^2}{R_{battery}}+P_{VF\varphi}V_I(1+2\cos\varphi)+P_{srds\varphi}V_I^2(1+2\cos\varphi)^2 \quad (24)$$

Denoting

$$a=P_{S\varphi}-P_{srds\varphi},\quad b=-P_{VF\varphi},\quad c=-\frac{V_{battery}^2}{R_{battery}}. \quad (25)$$

Equation (24) can be reduced to

$$aV_I^2(1+2\cos\varphi)^2+bV_I(1+2\cos\varphi)+c=0 \quad (26)$$

Here, we would like to obtain the minimum V_I that meets the charging power requirements. According to (3), when $\varphi=0$, a given I_P can be obtained with a minimum V_I. Then, (26) can be simplified to (27) to find out the minimum V_I,

$$9aV_I^2+3bV_I+c=0 \quad (27)$$

Equation (27) can be viewed as a normal quadratic equation with V_I as the variable. The input DC voltage V_I is derived as

$$V_I(k,V_{battery},R_{battery})=\frac{-b\pm\sqrt{b^2-4ac}}{6a}. \quad (28)$$

Since V_I should be positive, the negative solution is discarded and expression (29) is selected to represent V_I

$$V_I(k,V_{battery},R_{battery})=\frac{-b+\sqrt{b^2-4ac}}{6a}. \quad (29)$$

Fig. 4 shows the simulation results of the required minimum input DC voltage under varying coupling factor k, the battery equivalent resistance $R_{battery}$ and the respective charging $V_{battery}$. Fig. 4*a* is for three typical coupling factors k where $f_{resP}=82$ kHz, $f_{resS}=91$ kHz, $f_{OP}=88$ kHz, and $R_{battery}$ is from 7 to 30.4 Ω, and Fig. 4*b* is the three-dimensional surface under various k's. Although there are infinite resonant frequency combinations in their varying ranges discussed in Section 4 of the previous section, simulations for the extreme ones are enough to represent the whole thing. Figs. 4*c* and *d* depict the surfaces

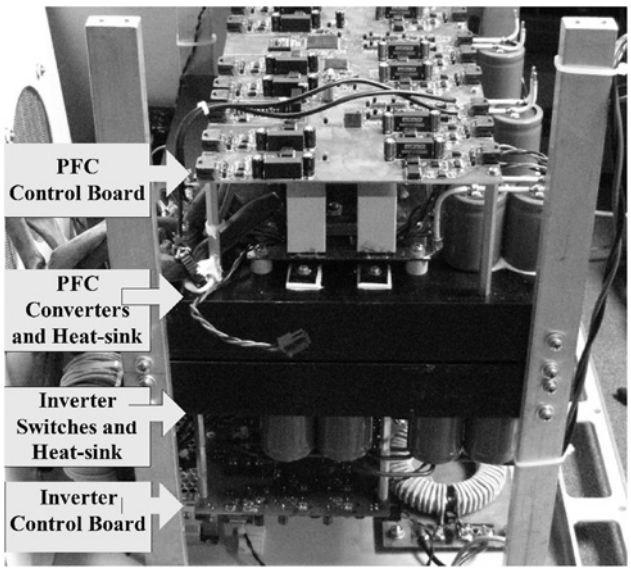

Fig. 6 *Laboratory prototype of the PFC and the phase-controlled inverter*

Table 2 Main parameters of wireless charging system for EVs

Parameter		Value
V_I	input DC voltage	400.0 V
M	mutual inductance between the primary and secondary coils	7.5 μH
f_{resP}	resonant frequency of the primary side	81.5 kHz
f_{resS}	resonant frequency of the secondary side	90.4 kHz
f_{OP}	operating frequency	88.0 kHz
L_P	inductance of coil at the primary side	32.7 μH
L_{Pline}	inductance of connection lines at the primary side	0.5 μH
C_P	capacitance of the primary side	115.1 nF
L_{mag}	magnetising inductances of three inter-cell transformers	32.1 μH 32.2 μH 31.9 μH
L_{leak}	leakage inductances of three inter-cell transformers	3.1 μH 3.0 μH 3.0 μH
r_{MOS}	ESR of the MOSFET	0.04 Ω
r_{ICT}	ESR's of inter-cell transformer windings	0.03 Ω
r_{CP}	ESR of the primary side resonant capacitor	0.01 Ω
r_{LP}	ESR of the primary side resonant inductor	0.06 Ω
t_r	raising time of the MOSFET	28 ns
t_f	falling time of the MOSFET	8 ns
L_S	inductance of coil at the secondary side	33.7 μH
L_{Sline}	inductance of connection lines at the secondary side	0.2 μH
C_S	capacitance of the secondary side	91.4 nF
r_{CS}	ESR of the secondary side resonant capacitor	0.01 Ω
r_{LS}	ESR of the secondary side resonant inductor	0.06 Ω
C_f	filter capacitance of the rectifier	300 μF
r_{Cf}	ESR of the secondary side filter capacitor	0.02 Ω
V_F	forward voltage of the secondary side rectifier diodes	0.7 V
R_F	ESR of the secondary side rectifier diodes	0.005 Ω

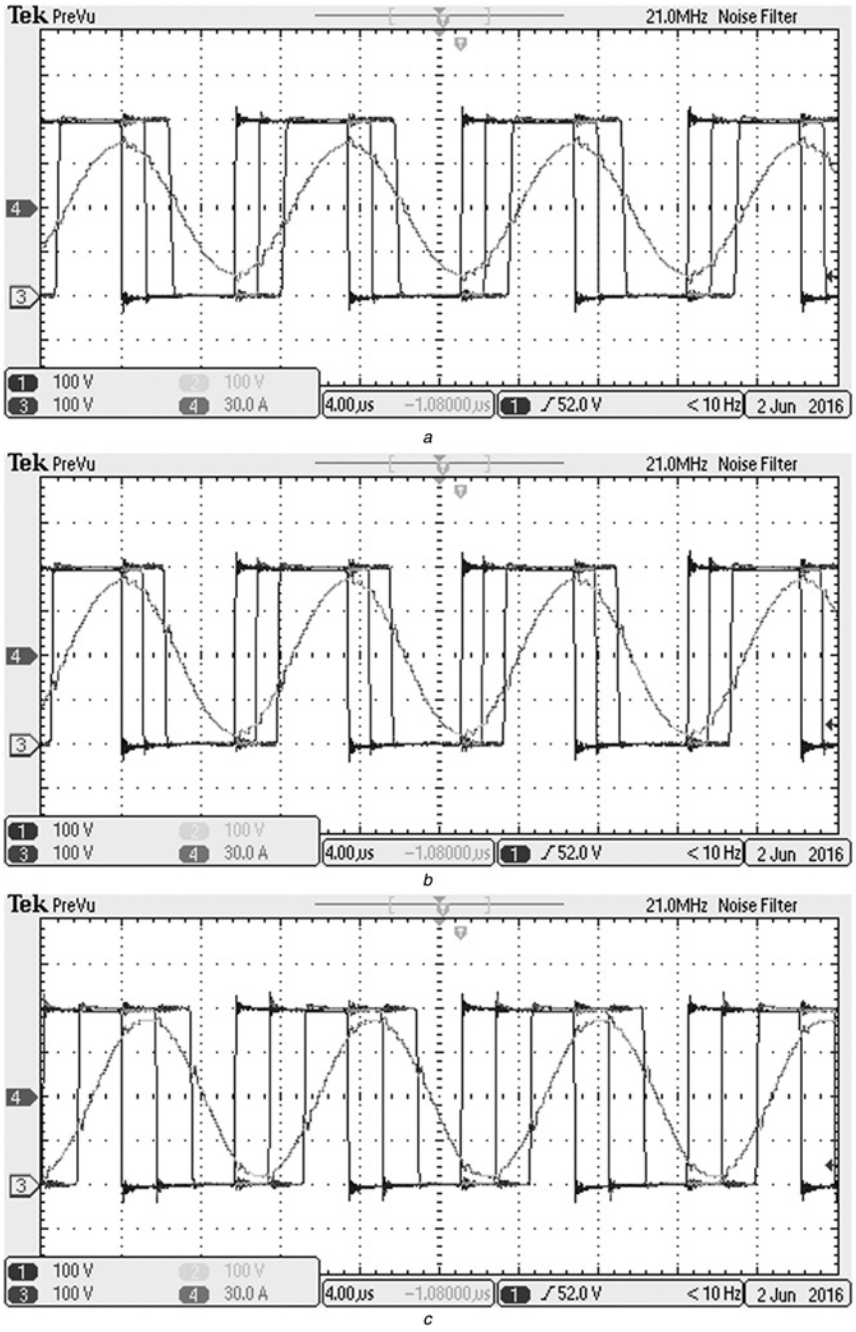

Fig. 7 *Experimental waveforms of three-phase output voltages and the total output current of the inverter for three typical battery equivalent resistances*

a For 7 Ω equivalent load at the constant current stage
b For 9.16 Ω equivalent load at the constant power stage
c For 30.4 Ω equivalent load at the constant voltage stage

under broader resonant frequency and battery resistance, which are detailed discussed in Section 4.4 of the previous section. As a result, voltage of 400 V is taken as the input DC voltage for inverters.

Figs. 4*b–d* show that the highest minimum required input DC voltage happens at the highest coupling factor together with the lowest equivalent battery resistance. Hence, a higher input DC voltage will be needed if an even higher coupling factor and/or lower equivalent battery resistance is required.

4.4 Phase-shift angle of the phase-controlled inverter

Due to the input DC voltage is set to 400 V, expression (26) can be simplified as

$$400^2 a(1+2\cos\varphi)^2 + 400b(1+2\cos\varphi) + c = 0. \tag{30}$$

Then the phase-shift angle of the phase-controlled inverter is deduced as

$$\varphi = \arccos\left(\left(\frac{-b+\sqrt{b^2-4ac}}{800a} - 1\right)/2\right). \tag{31}$$

Actually, there are two solutions of (30) and the negative solution is discarded.

4.5 Efficiency comparison

Under the nominal parameters (namely, $f_{\text{resP}} = 82$ kHz, $f_{\text{resS}} = 91$ kHz, $f_{\text{OP}} = 88$ kHz, R_{battery} is from 7 to 30.4 Ω, and $V_{\text{I}} = 400$ V), the phase angles can be calculated per (31), and power losses can

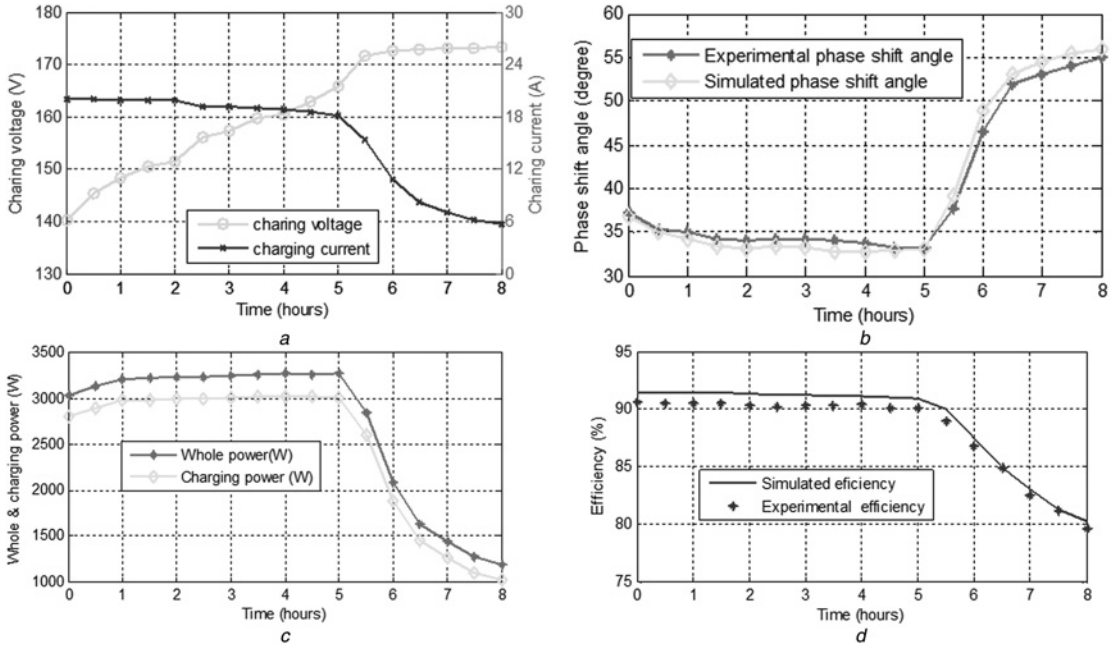

Fig. 8 *Experiment results for a typical wireless charging process*

a Current and voltage
b Phase-shift angle
c Charging power and total power
d Efficiency

be calculated using (14) and (17). As a result, the simulated efficiencies for respective k's are plotted in Fig. 5 with thick lines.

Before comparing the efficiency between the proposed topology and class-D inverters, the required input DC voltage for class-D ones should be determined. It is assumed that the series resonant topology is employed and the frequency control is used to regulate the output power for class-D inverters. Under the broader ranges of the resonant frequencies for both sides and the extended battery resistance, simulations show that the full-bridge class-D inverter with 155 V input DC voltage cannot provide enough required charging power sometimes while 160 V can. Hence 160 V is taken as the input DC voltage to conduct efficiency simulations for the full-bridge inverter. 315 V is taken for the half-bridge one via the same method. Assuming that all losses discussed above except inter-cell transformer ones are counted, the simulated efficiencies for the full-bridge topology and the half-bridge one are presented by thin lines in Figs. 5*a* and *b*, respectively. It can be seen that the phase controlled topology has higher efficiencies than class-D topologies under all cases. Especially, the efficiency improvement beyond 2% can always be obtained at the constant current stage as well as the constant power stage.

5 Experimental results

5.1 Prototype and parameters

The primary coil is the same as the secondary one in terms of dimensions: a rectangle 90 cm × 70 cm. Each coil contains four turns of litz wire. The litz wire type is AWG38, 2000 wires with an outer diameter of 6 mm. Six IPW65R041CFD MOSFET are employed to manufacture three half-bridge inverters. The rectifier was built using four VS-UFB280FA40 diodes. The prototype of the PFC and the inverter are built as shown in Fig. 6. Parameters of main components are listed in Table 2. Inductances, capacitances and coil ESR's are measured at the frequency of 88 kHz with an IET/QuadTech 7600 Precision LCR meters, and other components ESR's are obtained from manufacturer specifications. In order to get the preferred inductance, the coil is regulated through adjusting the space between adjacent turns with fixed dimensions of outmost sides.

5.2 Experimental results

The battery used in this experiment is a deep-cycle lead-acid battery US 8VGC XC, which is manufactured by the U.S. Battery Manufacturing Co., Ltd. Eighteen batteries are connected in series to provide a rated voltage of 144 V. The distance between the two axially aligned coils is about 20 cm. The measured mutual inductance is 7.5 μH which results in a coupling factor of $k = 0.226$ considering that inductances of the primary and secondary coils are 33.7 and 32.7 μH, respectively. The input DC voltage for the inverter is 400.0 V.

Fig. 7 shows three typical waveforms captured by an oscilloscope when the equivalent battery resistance varies during the charging process. Channels 1–3 measure output voltages of phases 1–3 and channel 4 is the total output current of the inverter. Figs. 7*a*–*c* obtained under the phase-shift angles of 37.3°, 33.7° and 54.9°, which corresponds to three typical charging stages (constant current, constant power and constant voltage), and battery equivalent resistances of 7, 9.16 and 30.4 Ω, respectively. It can be seen that all inverters maintain the ZVS condition under these scenarios, which matches with Fig. 3.

The whole charging time compromises three stages, i.e. constant current stage (first 2 h), constant power stage (next 3.5 h) and constant voltage stage (last 2.5 h). A simple bang-bang control is employed to regulate the charging voltage, current, and power. At the constant current stage, the charging current is regulated to 20 A ± 0.2 A till the charging power arrives at 3000 W. The charging power of 3000 W ± 15 W is maintained at the constant power stage before the battery voltage arrives at 173.2 V. At the constant voltage stage, the battery voltage is maintained at 173.2 V ± 0.8 V till the end when the charging current decreases to 5.7 A. Fig. 8*a* expresses the current and voltage of the experimental charging process.

Fig. 8*b* shows the experimental and simulated phase-shift angle for coupling factor $k = 0.226$, where the simulated one is plotted based on (31), resistances calculated based on measured voltages and currents of each half hour, and other parameters listed in Table 2. These two plots show a difference below 2° with the same trend.

Fig. 8*c* depicts the charging power and the total power output from the PFC. It shows that the charging power is slightly increasing from the beginning to the end of the constant power stage, being about 2.8 to 3.0 kW, and after that time the charging power is decreasing. The charging efficiency over 90% can be obtained at the stages of constant current and constant power.

Fig. 8*d* shows the experimental and simulated charging efficiencies versus charging time. These two plots show a 1% difference at most and practically share the same trend.

6 Conclusions

This paper focuses on the design and analysis of a wireless EVs charging system with a phase-controlled inverter. The charging power for an EV battery is regulated through adjusting the phase-shift angle among phases of the inverter. Detailed design procedure for major parameters, including the resonant and operating frequencies, and the coil dimensions are provided. The input DC voltage is determined considering the required charging power and power losses on both sides under various coil distances and equivalent battery resistances. The proposed system meets the required charging power and operates at ZVS conditions under varying parameters, including a broad range of charging distance of 12–25 cm, a variable equivalent battery resistance from 0.5 to 50 Ω for the typical three-stage charging process, and the resonant frequencies varying by ± 2.5% of the nominal ones at both sides.

An experimental 3.0 kW prototype was set up to validate the proposed system. Experiments show that the provided design considerations can reflect the system characteristics and can be used to design and analyse wireless EV charging systems.

7 Acknowledgment

This work was supported partly by the National Natural Science Foundation of China under Grant 51677139.

8 References

1 Keeling, N.A., Covic, G.A., Boys, J.T.: 'A unity-power-factor IPT pickup for high-power applications', *IEEE Trans. Ind. Electron.*, 2010, **57**, (2), pp. 744–751
2 Wang, C., Stielau, O.H., Covic, G.A.: 'Design considerations for a contactless electric vehicle battery charger', *IEEE Trans. Ind. Electron.*, 2005, **52**, (5), pp. 1308–1314
3 Huang, C.-Y., Boys, J.T., Covic, G.A., *et al.*: 'Practical considerations for designing IPT system for EV battery charging'. Proc. IEEE Vehicle Power and Propulsion Conf., September 2009, pp. 402–407
4 Wu, H.H., Gilchrist, A., Sealy, K., *et al.*: 'A high efficiency 5 kW inductive charger for EVs using dual side control', *IEEE Trans. Ind. Inf.*, 2012, **8**, (3), pp. 585–595
5 Seung-Hwan, L., Lorenz, R.D.: 'A design methodology for multi-kW, large air-gap, MHz frequency, wireless power transfer systems'. Proc. IEEE Energy Conversion Congress and Exposition, 2011, pp. 3503–3510
6 Sallan, J., Villa, J.L., Llombart, A., *et al.*: 'Optimal design of ICPT systems applied to electric vehicle battery charge', *IEEE Trans. Ind. Electron.*, 2009, **56**, (6), pp. 2140–2149
7 Elliott, G., Raabe, S., Covic, G.A., *et al.*: 'Multiphase pickups for large lateral tolerance contactless power-transfer systems', *IEEE Trans. Ind. Electron.*, 2010, **57**, (5), pp. 1590–1598
8 Covic, G.A., Boys, J.T., Tam, A.M.W., *et al.*: 'Self tuning pick-ups for inductive power transfer'. Proc. IEEE Power Electronics Specialists Conf., June 2008, pp. 3489–3494
9 Wu, H.H., Covic, G.A., Boys, J.T.: 'A series-tuned inductive-power-transfer pickup with a controllable AC-voltage output', *IEEE Trans. Power Electron.*, 2011, **26**, (1), pp. 98–109
10 Duan, C., Jiang, C., Taylor, A., *et al.*: 'Design of a zero-voltage-switching large-air-gap wireless charger with low electric stress for electric vehicles', *IET Power Electron.*, 2013, **6**, (9), pp. 1742–1750
11 Kandasamy, K., Vilathgamuwa, D.M., Madawala, U.K., *et al.*: 'Inductively coupled modular battery system for electric vehicles', *IET Power Electron.*, 2016, **9**, (3), pp. 600–609
12 Bojarski, M., Asa, E., Colak, K., *et al.*: 'A 25 kW industrial prototype wireless electric vehicle charger'. 2016 IEEE Applied Power Electronics Conf. and Exposition (APEC), March 2016, pp. 1756–1761
13 Choi, S., Huh, J., Lee, W.Y., *et al.*: 'New cross-segmented power supply rails for roadway powered electric vehicles', *IEEE Trans. Power Electron.*, 2013
14 Shin, J., Shin, S., Kim, Y., *et al.*: 'Design and implementation of shaped magnetic-resonance-based wireless power transfer system for roadway-powered moving electric vehicles', *IEEE Trans. Ind. Electron.*, 2014, **61**, (3), pp. 1179–1192
15 Thrimawithana, D.J., Madawala, U.K.: 'A generalized steady-state model for bidirectional IPT systems', *IEEE Trans. Power Electron.*, 2013, **28**, (10), pp. 4681–4689
16 Hao, H., Covic, G., Boys, J.: 'An approximate dynamic model of LCL-T-based inductive power transfer power supplies', *IEEE Trans. Power Electron.*, 2014, **29**, (10), pp. 5554–5567
17 Hao, H., Covic, G., Boys, J.: 'A parallel topology for inductive power transfer power supplies', *IEEE Trans. Power Electron.*, 2014, **29**, (3), pp. 1140–1151
18 Cai, H., Shi, L., Li, Y.-H.: 'Harmonic-based phase-shifted control of inductively coupled power transfer', *IEEE Trans. Power Electron.*, 2014, **29**, (2), pp. 594–602
19 Bac, N.X., Vilathgamuwa, D.M., Madawala, U.K.: 'A SiC-based matrix converter topology for inductive power transfer system', *IEEE Trans. Power. Electron.*, 2014, **29**, (8), pp. 4029–4038
20 Kazimierczuk, M.K., Czarkowski, D.: 'Phase-controlled resonant inverters', 'Resonant power converters' (Wiley – IEEE process, 2011, 2nd edn., ch. 11)
21 Bojarski, M., Czarkowski, D., Leon, F.D., *et al.*: 'Multiphase resonant inverters with common resonant circuit'. Proc. IEEE Int. Symp. on Circuits and Systems (ISCAS), June 2014, pp. 2445–2448
22 Czarkowski, D., Kazimierczuk, M.K.: 'Phase–controlled series–parallel resonant converter', *IEEE Trans. Power Electron.*, 1993, **PE–8**, pp. 309–319
23 Zheng, S., Czarkowski, D.: 'Modeling and digital control of a phase-controlled series-parallel resonant converter', *IEEE Trans. Ind. Electron.*, 2007, **54**, pp. 707–715
24 Deng, Q., Liu, J., Czarkowski, D., *et al.*: 'Frequency-dependent resistance of Litz-wire square solenoid coils and quality factor optimization for wireless power transfer', *IEEE Trans. Ind. Electron.*, 2016, **63**, (5), pp. 2825–2837